Check for updates

Positron annihilation lifetime, cation distribution and magnetic features of Ni$_{1-x}$Zn$_x$Fe$_{2-x}$Co$_x$O$_4$ ferrite nanoparticles

Hossein Nikmanesh, [ID] *[ab] Parviz Kameli,[a] Seyed Morteza Asgarian,[b] Shiva Karimi,[a] Mahmood Moradi,[b] Zohreh Kargar,[b] Joao Ventura, [ID] [c] Bernardo Bordalo[c] and Hadi Salamati[a]

A series of Zn and Co-substituted nickel ferrite nanoparticles of nominal composition Ni$_{1-x}$Zn$_x$Fe$_{2-x}$Co$_x$O$_4$ (x = 0, 0.1, 0.2, 0.3, 0.4, 0.5) have been synthesized by the PVA assisted sol–gel method. The reported structural and magnetic properties of the samples were investigated by X-ray diffraction (XRD), field emission scanning electron microscopy (FESEM), Fourier transform infrared spectroscopy (FTIR) and vibrating sample magnetometry (VSM). Also, the effect of these substitutions on vacancy distribution is investigated with positron annihilation lifetime spectroscopy (PALS). The cation distribution is inferred from the X-ray diffraction using the MAUD program to investigate ion occupancy, the exact coordinates of the atoms and unit cell dimensions. XRD analysis using the Rietveld refinement technique proves the crystalline structure and the growth of pure, single-phase and nanosize substituted nickel ferrite. These results are confirmed by the performed FESEM and FTIR studies. Magnetic measurements revealed that the values of the saturation magnetization (M_s) in the Ni$_{1-x}$Zn$_x$Fe$_{2-x}$Co$_x$O$_4$ samples gradually increased for doping levels up to x = 0.4, then decreasing for further content. Also, the coercivity showed an overall decreasing trend with increasing doping. The positron lifetime spectra of the substituted nickel ferrite were decomposed into three-lifetime components, τ_1, τ_2, τ_3. First of all, τ_1, is depends on the positrons that do not get trapped by the vacancy defects. The second lifetime component, τ_2, is attributed to positrons annihilation in vacancy-type defects in ferrite nanoparticles. The final lifetime, τ_3, is due to the annihilation of positrons across nanoparticles in the free volume of ferrite structure. Also, magnetic behaviors could be explained by positron annihilation lifetime spectroscopy.

1. Introduction

In recent years, spinel ferrites have been extremely studied for their effective application in microwave devices, information storage systems, sensors, loading coils, magnetic fluids and medical diagnostics.[1–6] Thus, much attention has been focused on the preparation and characterization of these materials.[6–8] Spinel ferrites have the general chemical formula $(A^{2+})[B_2^{3+}]O_4^{2-}$, where A^{2+} and B^{3+} are divalent (*i.e.* Co, Ni, Mn, Zn, …) and trivalent (*i.e.* Fe, Cr, …) cations occupying tetrahedral (A site) and octahedral (B site) interstitial positions of the fcc lattice formed by O^{2-} ions. As the cations in the two sites (A and B) are antiferromagnetically ordered, the magnetic properties observed in spinel ferrites are due to the unbalanced magnetic moments of the A and B sites. It is well known that the magnetic moment of the A and B sites depends on the cation distribution in these sites.[7–9] The knowledge of the cation distribution and spin alignment is essential to develop materials and to obtain the desired magnetic properties for the above-mentioned applications. In this regard, the investigation of the defect structure of nanosize ferrites is attracting a large amount of attention,[9–12] because of the significant role of vacancy-type defects in altering the electrical, magnetic and optical properties of bulk and nano-materials. Positron annihilation lifetime spectroscopy (PALS) is a sensitive technique for the characterization of the electronic structure and type and density of vacancy-type defects that can be straightforwardly and effectively applied in materials science, especially in spinel ferrites.[12]

One of the important class of spinel ferrites that is widely used in engineering and technology is nickel ferrite. Nickel ferrite (NiFe$_2$O$_4$) is a well-known inverse spinel ferrite in the bulk state with Ni^{2+} ions on B sites and Fe^{3+} ions distributed equally among A and B sites.[7] However, when nickel ferrite is synthesized at the nanoscale, it presents a mixed spinel structure with cations distributed on both A and B sites.[13–15] In

[a]Physics Department, Isfahan University of Technology, Isfahan 84156-83111, Iran. E-mail: h.nikmanesh@yahoo.com

[b]Physics Department, College of Sciences, Shiraz University, Shiraz 71946-84795, Iran

[c]IFIMUP, IN-Institute of Nanoscience and Nanotechnology, Departamento de Fisica, Faculdade de Ciencias, Universidade do Porto, Rua do Campo Alegre, 687, 4169-007 Porto, Portugal

addition, nickel–zinc ferrite is one of the soft magnetic materials which has large resistivity (10^6 Ω cm), high saturation magnetization, a high Curie temperature (570 °C), low coercivity and low dielectric.[16,17] Thus, the doping of metal ions in the nickel spinel structure may result to tune the structural, morphological, electrical and magnetic properties that lead to improve these properties for technological progress. For example, doping of nickel ferrites with zinc ions as a mixed spinel was studied by Rahimi and co-workers.[14] They showed that Zn^{2+} cations replaced Ni^{2+} in the tetrahedral sites so that the magnetic properties are changed. Thus, the saturation magnetization (M_s) initially increased for low doping levels but decreased with higher dopant concentration. Also, they showed that coercivity decreased by increasing Zn content due to the decrease of magnetocrystalline anisotropy constant. Saffari et al.[15] investigated the effects of Co-substitution on the magnetic properties of $NiCo_xFe_{2-x}O_4$ ferrites. They demonstrated that while M_s remained nearly constant with increasing Co^{3+}, the coercivity (H_c) increased significantly. Parvatheswara et al. studied the structure and magnetic behavior of nickel zinc cobalt ferrites. They reported that the cobalt substitution instead of zinc enhances the saturation magnetization while initial permeability decreases.[18] Generally, it would be useful if both saturation magnetization and coercivity could be held high or low upon the substitution. Thus, in view of the above discussions, the Zn–Co doped $Ni_{1-x}Zn_xFe_{2-x}Co_xO_4$ could show different magnetic behaviors that can be useful for various applications.

The present work deals with the cation distribution and magnetic properties of zinc–cobalt substituted nickel ferrite $Ni_{1-x}Zn_xFe_{2-x}Co_xO_4$ (x = 0, 0.1, 0.2, 0.3, 0.4, 0.5) synthesized by the PVA (polyvinyl alcohol) assisted sol–gel route. PALS was used to evaluate the vacancy type defects due to cobalt–zinc doped nickel ferrite. We attempt to find up a consistent correlation between the magnetic properties and the cation distribution and the defects concentration estimated by PALS in the prepared samples.

2. Experimental procedure

2.1. Samples preparation

Here, the polyvinyl alcohol (PVA) assisted sol–gel method was adopted for synthesizing Zn–Co substituted nickel ferrite samples. Iron nitrate ($Fe(NO_3)_3 \cdot 9H_2O$), nickel nitrate ($Ni(NO_3)_2 \cdot 6H_2O$), cobalt nitrate ($Co(NO_3)_2 \cdot 6H_2O$), zinc nitrate ($Zn(NO_3)_2 \cdot 4H_2O$), and PVA were taken as the raw materials and weighted according to the stoichiometric ratio. At first, the PVA solution was prepared by dissolving PVA powders in deionized water (3% w/v) at a temperature of about 80 °C until the solution became clear. At this point, and in order to avoid aggregation of the PVA in the water, the powder was slowly sprinkled in water under constant stirring. Then, the sols were prepared by dissolving all raw nitrate in deionized water. After constant stirring, the sols were added drop by drop to the clear PVA solution. This solution was then heated to 90 °C and treated in constant stirring for 24 h till a gel was obtained. The temperature of the gel was then increased to 140 °C for 2 h until the water

evaporated entirely and the gel was dried. Finally, the dried precursor was sintered at 800 °C for 4 h with heating rate 2 °C min^{-1}.

2.2. Samples characterization

X-ray diffraction (XRD) pattern of all samples was obtained on a Philips X'Pert Pro MPD X-ray diffractometer with Cu-Kα radiation (λ = 0.154 nm). We have employed the Material Analysis Using Diffraction (MAUD) program, version 2.54 for Rietveld analysis. It is designed to refine simultaneously both cation distribution and structural properties (lattice cell constants and atomic positions and occupancies). Positron annihilation lifetime measurements were performed using a slow–fast gamma–gamma coincidence spectrometer with time resolution (full width at half maximum; FWHM) of 250 ps for gamma rays emitted from a ^{60}Co source at room temperature. A total of about 10^6 coincidence events were collected in each lifetime spectrum. A source of strength ~15 μCi from $^{22}NaCl$ deposited on a Mylar foil with 7 μm thickness was used. The lifetime spectra were analyzed using the program Pasqual.[19] The source corrections were obtained with measurements on defect-free Al samples. The variances of all of the fitted positron annihilation lifetime spectra lied in a range of reasonable values, between 0.97 and 1.06. The morphology of the annealed samples was determined by field emission scanning electron microscopy (FESEM; model S-4160). Also, the analysis of the samples formation was done using Fourier transform infrared spectroscopy (FTIR; Jasco 860 plus). Finally, magnetic hysteresis loops of the samples were recorded using a vibrating sample magnetometer (VSM; Lake Shore 7307) with a maximum field of ±10 kOe.

3. Results and discussions

3.1. X-ray diffraction analysis

The X-ray diffraction spectra of $Ni_{1-x}Zn_xFe_{2-x}Co_xO_4$ (x = 0, 0.1, 0.2, 0.3, 0.4, 0.5) are shown in Fig. 1. The entire XRD patterns show the reflections belonging to cubic spinel structure with space group $Fd3m$ and no extra peaks have been observed in the
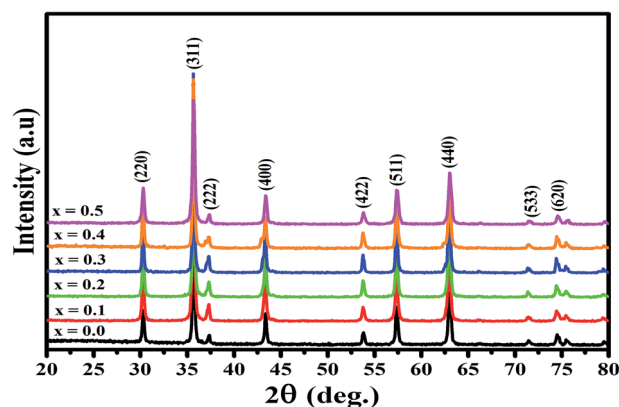

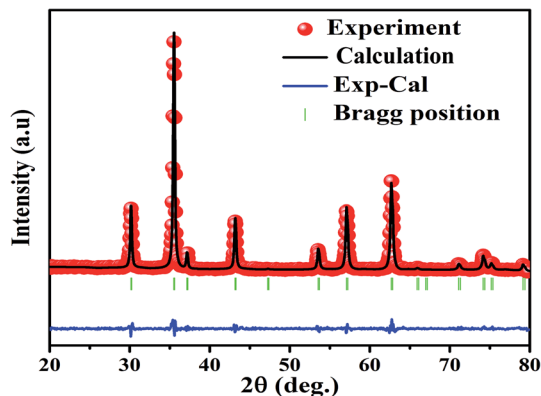Fig. 1 XRD patterns of the $Ni_{1-x}Zn_xFe_{2-x}Co_xO_4$ (x = 0, 0.1, 0.2, 0.3, 0.4, 0.5) samples.

Fig. 2 XRD pattern refinement using MAUD software for the $Ni_{0.5}$-$Zn_{0.5}Fe_{1.5}Cr_{0.5}O_4$ sample.

Table 1 Variation of the lattice parameter were obtained using MAUD, Reitveld agreement factors ($R_{wp} - R_{exp} - \chi$), mean ionic radii (r_A, r_B) and theoretical lattice parameter (a_{th}) for $Ni_{1-x}Zn_xFe_{2-x}Co_xO_4$ samples

X	a_{MAUD} (Å)	a_{th} (Å)	R_{wp}	R_{exp}	χ	r_A (Å)	r_B (Å)
$x = 0$	8.3752	8.3756	15.42	11.81	1.32	0.5188	0.7305
$x = 0.1$	8.3798	8.3791	18.17	12.53	1.45	0.5313	0.7292
$x = 0.2$	8.3777	8.3772	22.56	12.74	1.76	0.5313	0.7261
$x = 0.3$	8.3801	8.3800	21.92	12.45	1.76	0.5374	0.7355
$x = 0.4$	8.3776	8.3773	19.62	12.04	1.62	0.5409	0.7348
$x = 0.5$	8.3718	8.3714	17.11	12.42	1.37	0.5410	0.7341

XRD patterns. The crystal structures were obtained using the MAUD program. The fitting quality of the experimental data was checked by weighted profile R-factor (R_{wp}), the expected R-factor (R_{exp}), and the goodness of the fit $\left(\chi = \frac{R_{wp}}{R_{exp}} \right)$.[20] In this fitting process, crystal lattice constant and cation distribution were determined. Fig. 2 shows a typical Rietveld analysis for the $Ni_{0.5}Zn_{0.5}Fe_{1.5}Co_{0.5}O_4$ sample. In Table 1 and Fig. 3 are shown the variation of the lattice constant obtained from the MAUD

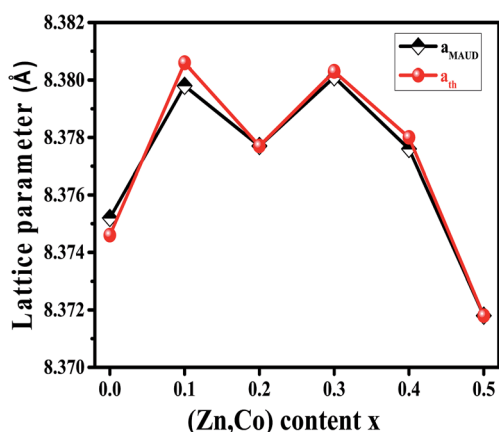**Fig. 3** Variation of lattice parameter obtained by MAUD and theoretical lattice parameter of $Ni_{1-x}Zn_xFe_{2-x}Co_xO_4$ samples.

program. The values of the lattice parameter 'a' are almost constant, but do not show a regular trend with increasing Zn–Co content, due to the different type of cation distribution and ionic radii in the doped-samples. The initial increase of lattice parameter can be related to the replacement of the smaller Ni^{2+} ions (0.55 Å, 0.69 Å) by the larger Zn^{2+} ions (0.60 Å, 0.74 Å)[21] in A and B sites. Also, the decrease of lattice parameter above $x = 0.3$ can be caused by the replacement of larger Fe^{2+} ions (0.63 Å, 0.78 Å) by smaller Co^{2+} ions (0.58 Å, 0.74 Å) in A and B sites. In addition, a fraction of the B sites is occupied by Co^{3+} instead of Fe^{3+} ions. Therefore, the different ionic radii of the cations and the type of ions occupying A and B sites can result in the enhancement or reduction of the lattice parameters.

3.2. FESEM morphology

The morphology and microstructure of the samples were studied by FESEM images. The FESEM images of $NiFe_2O_4$ and $Ni_{0.5}Zn_{0.5}Fe_{1.5}Cr_{0.5}O_4$ samples are shown in Fig. 4. The images show that particles are in the nanometer range (with average particle size about 60 nm), nearly spherical in shape and a tendency for agglomerated due to crystal growth and their magnetic interactions. Also, zinc and cobalt substituted in nickel ferrite overall seemed to have no effect on particle size.

3.3. Cations distribution

The physical properties of ferrites are sensitive to the nature, valence and distribution of cations over the A and B sites. Thus, the knowledge and obtaining of suitable cation distribution can be helpful to understand the behavior of their magnetic and electrical properties.

To determine the mechanism of Zn–Co substitution in $Ni_{1-x}Zn_xFe_{2-x}Co_xO_4$, the following three assumptions were considered. First of all, structural refinements were looked for, assuming that Zn^{2+} ions occupied A and B sites. The second assumption was that Co^{2+} ions went into both A and B sites (because of the preference position of Co^{2+}).[22] In the third assumption, we considered that Co^{3+} existed in the B sites because of charge valence, lattice parameter and magnetic properties. In fact, to confirm these assumptions, we calculated the mean ionic radii of A and B sites (r_A and r_B) for all the samples:[23]

$$r_A = \sum_i r_i \alpha_i, \quad r_B = \frac{1}{2} \sum_i r_i \alpha_i \qquad (1)$$

where α_i is the concentration of the element i with ionic radius r_i on the respective site. The values of r_A and r_B are reported in Table 1. It is observed that r_A increases but r_B changes non-monotonously with increasing Zn–Co substitution. The enhancement of r_A is related to the replacement of smaller Ni^{2+} ions by Zn^{2+} with larger ionic radii in the A sites. The variation of r_B depends on the replacement by Zn^{2+}, Co^{2+} and Co^{3+} in the B sites. The theoretical lattice constant (a_{th}) was calculated using:[24]

$$a_{th} = \frac{8}{3\sqrt{3}} \left[(r_A + R_0) + \sqrt{3} (r_B + R_0) \right] \qquad (2)$$

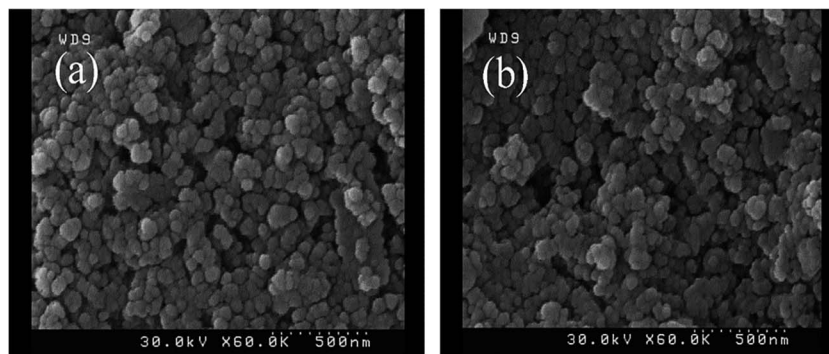**Fig. 4** FESEM images of the $Ni_{1-x}Zn_xFe_{2-x}Co_xO_4$ ((a) $x = 0.0$ and (b) $x = 0.5$) samples.

where R_0 is the radius of oxygen. Thus, we calculated a_{th} and compared it with the value of 'a' extracted from the MAUD refinement (a_{MAUD}; Fig. 3). We can conclude that a_{th} and a_{MAUD} are in good agreement with each other. Thus, we considered the cation distribution that is shown in Table 2.

3.4. Positron annihilation lifetime spectroscopy

The positron annihilation lifetime spectra of the $Ni_{1-x}Zn_x$-$Fe_{2-x}Co_xO_4$ ($x = 0.0$, 0.1, 0.2, 0.3, 0.4 and 0.5) ferrites were resolved into three components τ_1, τ_2 and τ_3 with their relative intensities I_1, I_2 and I_3, respectively. The variation of the lifetime components and their intensities *versus* x are shown in Fig. 5. The smallest lifetime component (τ_1) is related to the annihilation of positrons that do not get trapped by the defects within the samples and a small contribution from the result of Bloch state residence time of trapped positrons.[25] Also, the para-positronium formation in the samples with lifetime 125 ps and intensity of one-third of the orthopositronium intensity I_3 has a negligibly small contribution in this component.

The lifetime component τ_2 is due to annihilation of positrons in vacancy type defects within the grain and the grain surface of the samples. The reported diffusion length of positrons in oxide materials is between 10–60 nm (ref. 26–28) and also diffusion length decrease with increasing in trapping site density.[29,30] Therefore, since in these nanoparticles, the trapping site density (cationic vacancies of A and B sites) is high, the mean diffusion length of positrons in sample nanoparticles is a few nanometers. Consequently, we expect that more positrons annihilate in the grains of the nanoparticles. In nanoferrites, the lifetime component τ_2 is mainly due to the annihilation of positrons in vacancies of the A and B sites.[10,31,32] In the spinel structure, oxygen anions

form octahedral (B) sites surrounded by six oxygen ions and tetrahedral (A) sites occupied by metallic cations surrounded by four oxygen ions. Therefore, the B sites have more minus charge and are bigger than the A sites. These sites can trap positrons and the lifetime of positrons in B sites is smaller than A sites. Therefore, from Fig. 5 it can be deduced that, for the $x = 0.0$ until $x = 0.3$ samples, more positrons are annihilated in the A sites, while for the $x = 0.4$ and 0.5 samples, more positrons are annihilated in the B sites. As it is shown in Table 1 for $x = 0.0$ sample, since the radius of Ni^{2+} (0.55 Å in A sites) and Fe^{2+} (0.61 Å in A sites) are bigger than the radius of A sites (0.5188 Å), some of the cations do not occupy A sites and form monovacancies in tetrahedral sites. This behavior is similar for the $x = 0.1$, 0.2 and 0.3 samples, a number of A sites are not occupied with cations because the cation radius is larger than the tetrahedral radius. For the $x = 0.4$ and 0.5 samples, the radius of the A site increased whereas the radius of the B site decreased (Table 1). Because of the larger radius of the Zn^{2+} and Co^{2+} ions in the A sites, they occupy A sites by pushing the oxygen atoms along the body diagonals of octants of the spinel structure. This causes the shrinkage of the octahedral sites and some of the metallic cations may leave B sites as monovacancies and do not occupy these sites. Therefore, the cationic vacancies decreased in A sites and increased in B sites and the cationic vacancies at the B sites became the predominant trapping centers for positrons. Since B site has more minus charge than the A site, the positron lifetime decreases. Also, the small decrease in τ_2 for the $x = 0.1$ and 0.2 samples compared to the $x = 0.0$ and 0.3 can be due to the increase in the number of cationic vacancies in the B sites because of decreasing in the radius of B sites (r_B).

The intensity of I_2 increases with increasing in x content. This is due to the larger radius of Zn^{2+} and Co^{2+} compare to Ni^{2+}

Table 2 Cation distribution in A and B sites for $Ni_{1-x}Zn_xFe_{2-x}Co_xO_4$ samples

| X	Tetrahedral sites (A)	Octahedral sites (B)
$x = 0.0$	$(Ni_{0.13}{}^{2+}Fe_{0.72}{}^{3+}Fe_{0.15}{}^{2+})$	$(Ni_{0.82}{}^{2+}Ni_{0.05}{}^{3+}Fe_{0.12}{}^{3+}Fe_{1.01}{}^{2+})$
$x = 0.1$	$(Ni_{0.11}{}^{2+}Zn_{0.1}{}^{2+}Fe_{0.61}{}^{3+}Fe_{0.15}{}^{2+}Co_{0.03}{}^{2+})$	$(Ni_{0.76}{}^{2+}Ni_{0.03}{}^{3+}Fe_{0.12}{}^{3+}Fe_{1.01}{}^{2+}Co_{0.06}{}^{2+}Co_{0.01}{}^{3+})$
$x = 0.2$	$(Ni_{0.1}{}^{2+}Zn_{0.14}{}^{2+}Fe_{0.6}{}^{3+}Fe_{0.11}{}^{2+}Co_{0.05}{}^{2+})$	$(Ni_{0.67}{}^{2+}Ni_{0.03}{}^{3+}Zn_{0.06}{}^{2+}Fe_{0.12}{}^{3+}Fe_{0.95}{}^{2+}Co_{0.13}{}^{2+}Co_{0.02}{}^{3+})$
$x = 0.3$	$(Ni_{0.1}{}^{2+}Zn_{0.2}{}^{2+}Fe_{0.54}{}^{3+}Fe_{0.1}{}^{2+}Co_{0.06}{}^{2+})$	$(Ni_{0.57}{}^{2+}Ni_{0.03}{}^{3+}Zn_{0.1}{}^{2+}Fe_{0.11}{}^{3+}Fe_{0.95}{}^{2+}Co_{0.21}{}^{2+}Co_{0.03}{}^{3+})$
$x = 0.4$	$(Ni_{0.09}{}^{2+}Zn_{0.23}{}^{2+}Fe_{0.5}{}^{3+}Fe_{0.08}{}^{2+}Co_{0.1}{}^{2+})$	$(Ni_{0.48}{}^{2+}Ni_{0.03}{}^{3+}Zn_{0.17}{}^{2+}Fe_{0.11}{}^{3+}Fe_{0.91}{}^{2+}Co_{0.23}{}^{2+}Co_{0.07}{}^{3+})$
$x = 0.5$	$(Ni_{0.08}{}^{2+}Zn_{0.25}{}^{2+}Fe_{0.49}{}^{3+}Fe_{0.05}{}^{2+}Co_{0.13}{}^{2+})$	$(Ni_{0.39}{}^{2+}Ni_{0.03}{}^{3+}Zn_{0.25}{}^{2+}Fe_{0.11}{}^{3+}Fe_{0.85}{}^{2+}Co_{0.27}{}^{2+}Co_{0.1}{}^{3+})$
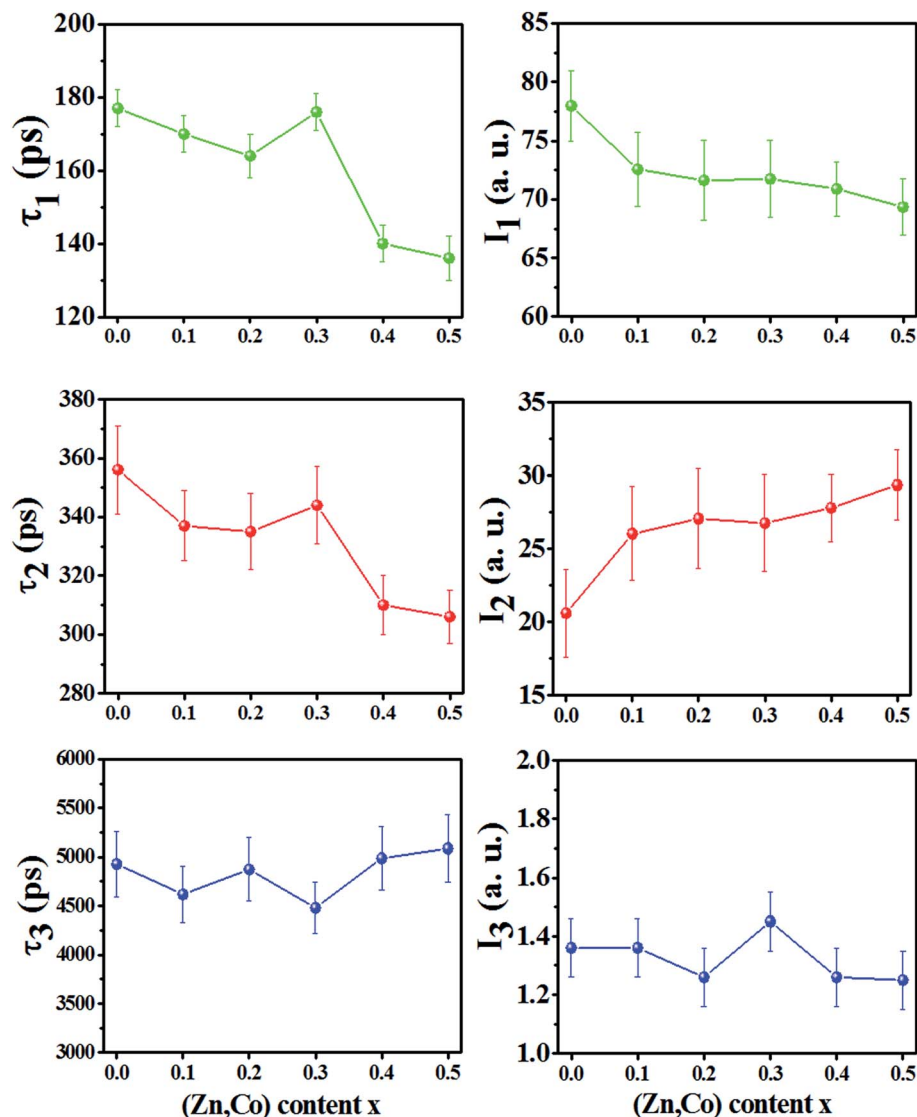
Fig. 5 Variation of positron lifetime components and their intensities *vs.* x content for $Ni_{1-x}Zn_xFe_{2-x}Co_xO_4$ samples.

and Fe^{3+} cations. This show that the number of vacancies in the samples increases with increasing x.

The nanosecond component τ_3, is indicative of the formation of orthopositronium (O-Ps) atoms in the large free volumes in the intergranular regions of the nanoparticles. O-Ps atoms in materials were annihilated through "pick-off" process and their lifetime reduced from 140 ns in vacuum to typically 1–5 ns. The variation of τ_3 and its very small intensity (~1.3%) is due to the agglomeration of nanoparticles in powder and does not reflect the effects of any change in the number of vacancies within the nanoparticles due to the x content.

The cumulative effect of all of the positron annihilations in the samples can be studied using the mean positron lifetime, τ_m, defined as:[25,31–33]

$$\tau_m = \frac{\tau_1 I_1 + \tau_2 I_2 + \tau_3 I_3}{I_1 + I_2 + I_3} \quad (3)$$

Because of a large number of counted coincidence events and the stability of the positron annihilation lifetime spectrometer, τ_m has a high statistical accuracy.[33] The mean positron annihilation lifetime of the samples as a function of x (Zn and Co content) is shown in Fig. 6. As shown, the τ_m for the x = 0.0–0.3 samples is larger than for the x = 0.4 and 0.5 samples, confirming the annihilation of most of the positrons in A sites for the x = 0.0–0.3 samples and in the B sites for the x = 0.4 and x = 0.5 samples. Since A sites have smaller minus charge than B sites, the mean positron lifetime in A sites is larger than in B sites.

3.5. FTIR spectroscopy

The Fourier transform infrared spectroscopy (FTIR) spectrum were recorded at 300 K in the wave number range of 380–7800 cm^{-1}. The spectra for the samples as a function of Zn–Co substitution are shown in Fig. 7. Two main absorption bands
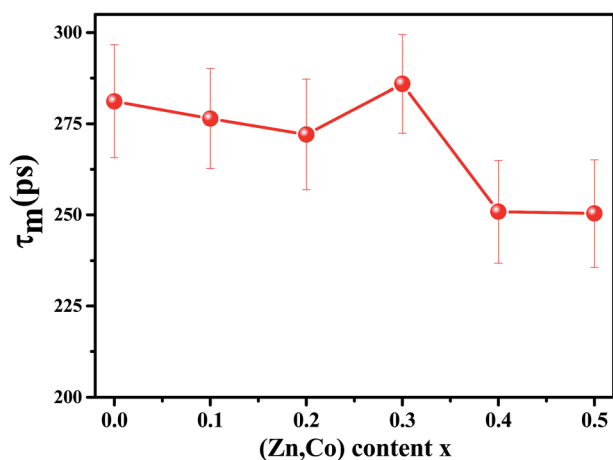
Fig. 6 Variation of mean positron lifetime (τ_m) vs. x for $Ni_{1-x}Zn_x$-$Fe_{2-x}Co_xO_4$ samples.

are observed between 399–610 cm^{-1}. The high frequency band, ν_1 (590–610 cm^{-1}) is a referenced stretching vibration of the cation–anion band in tetrahedral sites (A), while the low frequency band, ν_2 (400–420 cm^{-1}) corresponds to the stretching vibration of the cation–anion band in octahedral sites (B).[34] Therefore, these two bands ν_1 and ν_2 confirm the formation of a spinel ferrite structure.[35] The degree of covalent bonding determines the band position for the A and B sites. Actually, the Fe–O distance at the A sites is smaller than at the B sites. Therefore, covalent banding of Fe–O in A sites is stronger than B sites.[36] It can be concluded that vibration stretching of tetrahedral sites occurs in higher wave number. The variation of the band position of ν_1 and ν_2 are shown in Fig. 7. The slight shift in the ν_1 and ν_2 peak position for the samples might be due to the distribution of Zn^{2+}, Co^{2+} and Co^{3+} which replace Ni^{2+}, Fe^{2+} and Fe^{3+} ions and to the distribution creation of vacancies in samples observed in the 'Positron annihilation lifetime spectroscopy' study. The reduction of the ν_1
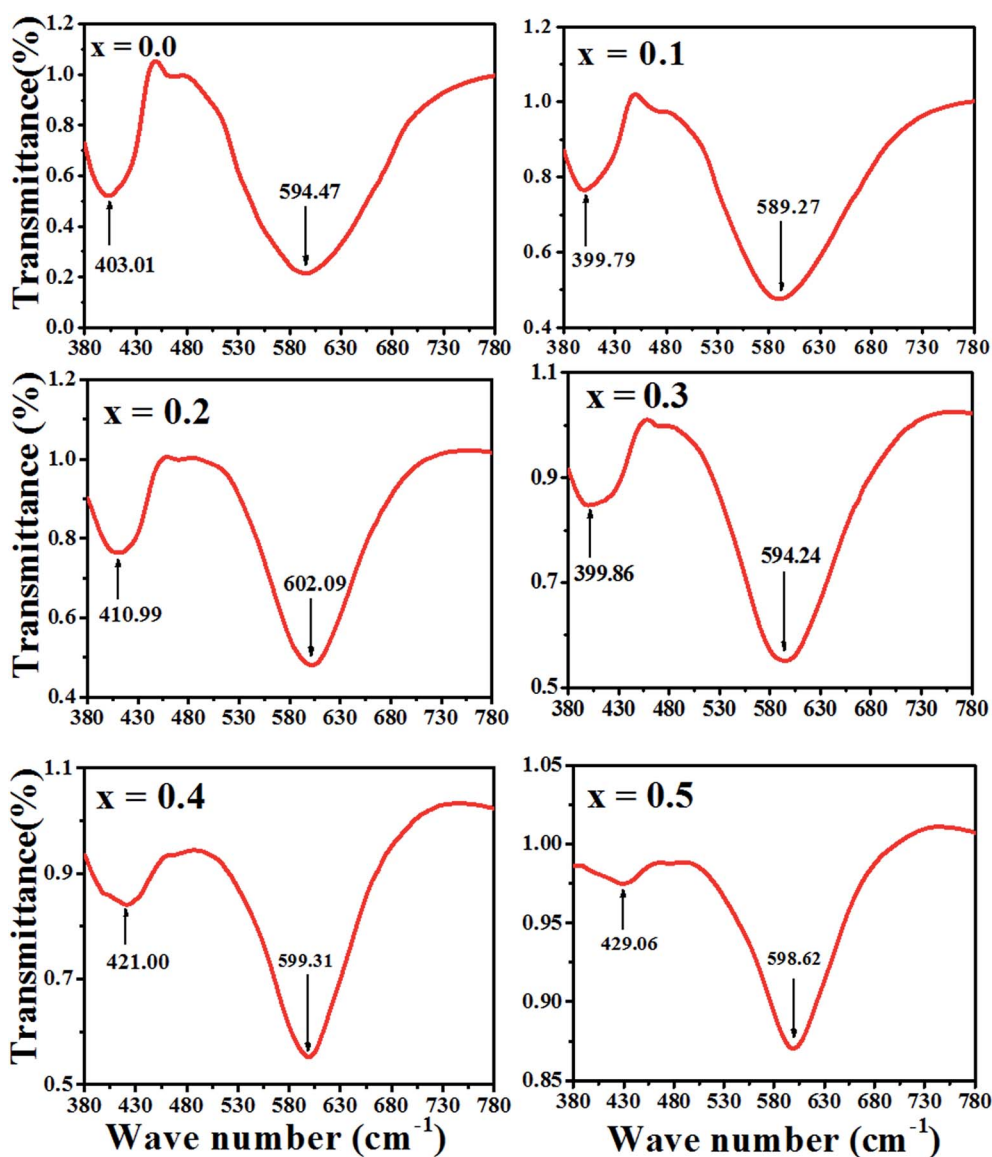

Fig. 7 FTIR spectra of $Ni_{1-x}Zn_xFe_{2-x}Co_xO_4$ samples.
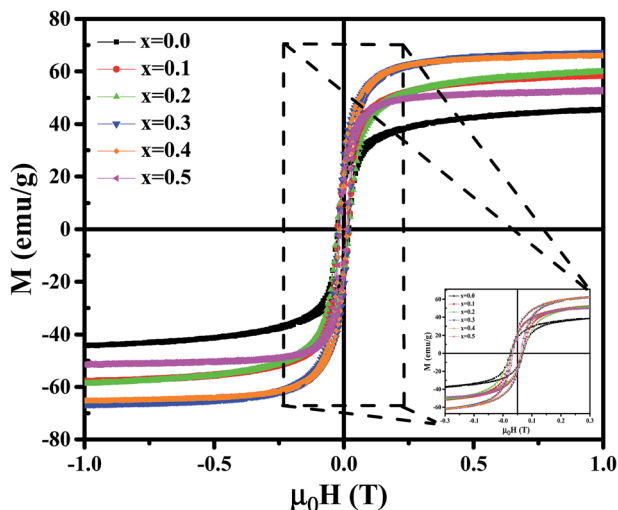
Fig. 8 The $M–H$ loops for $Ni_{1-x}Zn_xFe_{2-x}Co_xO_4$ samples.

and v_2 depth intensities for two samples of $x = 0.4$ and 0.5 can be due to the increase in vacancies in these samples, as shown with I_2 in Fig. 5.

3.6. Magnetic properties

Magnetic properties of $Ni_{1-x}Zn_xFe_{2-x}Co_xO_4$ ($x = 0, 0.1, 0.2, 0.3, 0.4, 0.5$) ferrites were evaluated using VSM and the results of the hysteresis curves of all samples are shown in Fig. 8. From this figure, the values of saturation magnetization (M_s), remanent magnetization (M_r) and coercivity (H_c) were estimated and tabulated in Table 3. It can be seen that M_s initially increased with increasing doping level up to $x = 0.4$, decreasing for further content. This behavior can be explained by the cation distribution on the basis of the experimental data of magnetization and lattice parameters. The observed magnetic moment per unit formula n_B^{exp} in units of Bohr magneton was obtained from:[23]

$$n_B^{exp} = \frac{M_w M_s}{5585} \tag{4}$$

where, M_w is the molecular weight of the samples. In addition, we calculated the theoretical magnetic moment $n_B^{cal} = M_B - M_A$,[37] where M_A and M_B are the A-site and B-site sub-lattice magnetic moments estimated from the magnetic moment of each element in terms of the Bohr magneton μ_B (5, 4, 0, 3, 2, 3 and 4 for Fe^{3+}, Fe^{2+}, Zn^{2+}, Ni^{3+}, Ni^{2+}, Co^{2+} and Co^{3+} respectively)

and the estimated cation distributions at the A and B sites. Fig. 9 shows n_B^{cal} and n_B^{exp} for the $Ni_{1-x}Zn_xFe_{2-x}Co_xO_4$ samples. A good agreement is observed between n_B^{exp} and n_B^{cal} for $x \leq 0.3$. The incompatibility of n_B^{exp} and n_B^{exp} for $x = 0.4$ and $x = 0.5$ is due to non-magnetic Zn^{2+} ions occupying the A sites replacing Fe^{3+} and the fractional Zn^{2+} ions occupying Fe^{2+}. Thus, the net magnetic moment increased with increasing Zn^{2+} due to the larger reduction in the magnetic moment of A sites compared to those of B sites. The reduction in n_B^{exp} beyond $x = 0.3$ is due to the fact that the magnetization of the A sub-lattice becomes weaker than that of the B sites and, therefore, the A–B exchange interaction becomes weaker or comparable with the B–B exchange interaction, which would then disturb the collinear spin structure in the system at the B sites.[38,39]

For a more thorough explanation of the magnetic behavior of Zn–Co substitution in Ni ferrites, we considered separately the magnetic behavior of $Ni_{1-x}Zn_xFe_2O_4$ and $NiFe_{2-x}Co_xO_4$ samples which have been reported previously.[14,15] In $Ni_{1-x}Zn_xFe_2O_4$, it was observed that the saturation magnetization initially increased up to $x = 0.3$ and decreases for further content, which can be explained by two-Neel's sub-lattice model. Non-magnetic Zn^{2+} ions are occupying A sites and fractional Zn^{2+} ions are occupying B sites replacing Ni^{2+}. So Fe^{3+} and Fe^{2+} migrated in both sites. Thus, the net magnetic moment increased with
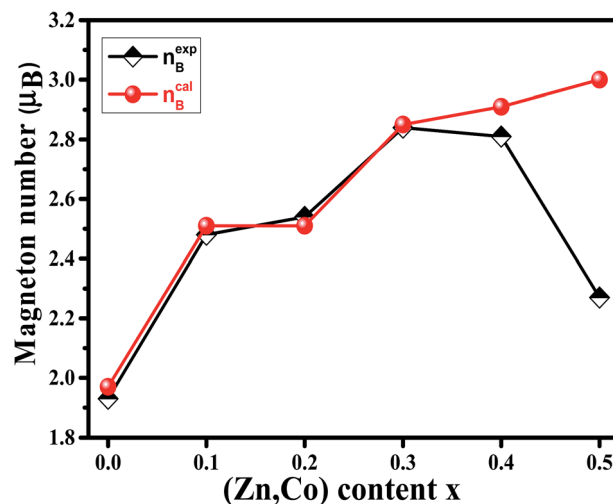

Fig. 9 Variation of calculated (n_B^{cal}) and experimental (n_B^{exp}) magneton number of $Ni_{1-x}Zn_xFe_{2-x}Co_xO_4$ samples.

Table 3 Saturation magnetization (M_s), coercivity (H_c), remanence magnetization (M_r), anisotropy constants (K_1), n_B^{exp} and n_B^{cal} for $Ni_{1-x}Zn_xFe_{2-x}Co_xO_4$ samples

X	M_s (emu g^{-1})	M_r (emu g^{-1})	H_c (T)	$R = \dfrac{M_r}{M_s}$	n_B^{exp} (μ_B)	n_B^{cal} (μ_B)	K_1 (erg cm^{-3}) $\times 10^3$
$x = 0$	46	18	0.019	0.39	1.93	1.97	191.9
$x = 0.1$	59	21	0.018	0.35	2.48	2.51	167.7
$x = 0.2$	60	19	0.02	0.31	2.54	2.51	205.5
$x = 0.3$	67	22	0.016	0.32	2.84	2.85	161.3
$x = 0.4$	66	17	0.011	0.25	2.81	2.91	127.8
$x = 0.5$	53	20	0.01	0.37	2.27	3.00	89.5

increasing Zn^{2+} due to the larger reduction in the magnetic moment of A sites compared to those of B sites.

In $NiFe_{2-x}Co_xO_4$, VSM result demonstrated that M_s remained nearly constant with increasing Co^{3+} substitution. The observed slight changes in M_s might be due to the type of cation distribution, which can be explained by Co^{3+} occupying both A and B sites. By comparing the behavior of M_s in the two above systems, it can be concluded that the here observed behavior of the saturation magnetization in $Ni_{1-x}Zn_xFe_{2-x}Co_x-O_4$ is between the two.

To justify the behavior of $Ni_{1-x}Zn_xFe_{2-x}Co_xO_4$, one should consider the cation distribution, PALS and Neel's two sub-lattice model. According to the Neel's model, the magnetic ordering in the spinel ferrites is based on the Neel's two sub-lattices (A-sites and B-sites) and the resultant magnetization is the difference between magnetization of octahedral site (B-site) and tetrahedral site (A-site), provided that they are collinear and anti-parallel to each other. For the $x = 0.1$, 0.2 and 0.3 samples, some cations do not occupy the A sites and therefore mono-vacancies could form. So, the magnetization of the A sites will be smaller than that of B sites. Also, since the Zn^{2+} ion has no magnetic moment, the net magnetic moment is increased with increasing Zn content due to a decrease in fraction of magnetic moment of A site and an increase in the net magnetic moment of B sites. By considering Neel's model, it can be concluded that the saturation magnetization increases until $x = 0.3$. After that, the net magnetic moment decreases for $x = 0.4$ and $x = 0.5$. This may be due to the weakening of A–B exchange interactions, decreasing the number of magnetic linkages occurring between tetrahedral (A) and octahedral (B) cations. In addition, it can be related to an increase in the number of cation vacancies in these two samples that, as argued in Section 3.4, are mainly distributed in the B sites.

It is evident from Table 3, that the coercivity gradually decreases except for $x = 0.2$. To describe the process of coercivity, we use:[40]

$$H_c = \frac{2K_1}{\mu_0 M_s} \quad (5)$$

where K_1 is the cubic anisotropy constant given by $K_1 = \mu_0 M_s \sqrt{\frac{105b}{8}}$ (where b is due to the crystal anisotropy), M_s is the saturation magnetization (the magnetization near M_s can be written by $M = M_s \left(1 - \frac{b}{H^2}\right)$) and μ_0 is the permeability of free space.[22,37]

Firstly, the room temperature experimental data M vs. H were fitted by equation $\left(M = M_s \left(1 - \frac{b}{H^2}\right)\right)$ and the value of b and M_s were obtained and used to calculate K_1. The obtained values of K_1 are reported in Table 3. It is observed that the anisotropy constant decreased, which leads to the decrease in coercivity except for $x = 0.2$, as shown in Fig. 10. This figure shows a good agreement between the coercivity and anisotropy constant values for the $Ni_{1-x}Zn_xFe_{2-x}Co_xO_4$ samples.

The overall change (decrease with increase in x value) of the coercivity and anisotropy are similar to the overall change of the
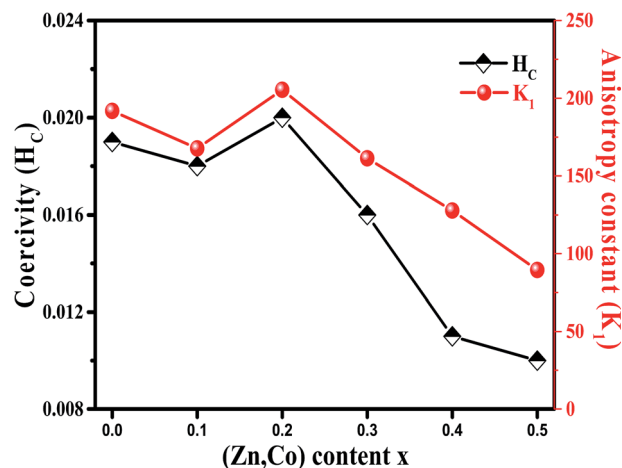

Fig. 10 Variation of coercivity (H_c) and anisotropy constant (K_1) for $Ni_{1-x}Zn_xFe_{2-x}Co_xO_4$ samples.

mean positron lifetime, τ_m. As shown in Fig. 5 and 10, the samples that have higher τ_m, have larger anisotropy constant. Since τ_m is proportional to electron density of vacancy, therefore the vacancies with less the electron density may cause larger anisotropy constant.

4. Conclusions

In this work, $Ni_{1-x}Zn_xFe_{2-x}Co_xO_4$ ($x = 0$, 0.1, 0.2, 0.3, 0.4, 0.5) nanoparticles ferrites were synthesized by sol–gel method using PVA as surfactant. The FESEM images showed that the particles were in the nanosize range. XRD and FTIR analysis confirmed the formation of a spinel ferrite structure and Rietveld refinements using the MAUD program based on XRD gave the cation distributions in all of the samples. The investigations of defects in the samples were carried out using positron lifetime spectroscopy. According to positron annihilation, the dominant of vacancies in $x = 0.0$–0.3 samples are cationic vacancies in A sites whereas for $x = 0.4$ and 0.5 samples, cationic vacancies in B sites are mainly predominant. Also, the number of vacancies increases with increasing x content. A good agreement is observed between n_B^{exp} and n_B^{cal} for the prepared samples. The obtained values of anisotropy constant decreased with increasing dopant content except in the $x = 0.2$ sample, consistent with the coercivity values. Also, the overall change of the coercivity and anisotropy are similar to the overall change of the mean positron lifetime.

References

1 R. C. Pullar, *Prog. Mater. Sci.*, 2012, **57**, 1191–1334.
2 M. Y. Nassar and M. Khatab, *RSC Adv.*, 2016, **6**, 79688–79705.

3 Y. Xu, D. Sun, H. Hao, D. Gao and Y. Sun, *RSC Adv.*, 2016, **6**, 98994–99002.

4 W. Hu, N. Qin, G. Wu, Y. Lin, S. Li and D. Bao, *J. Am. Chem. Soc.*, 2012, **134**, 14658–14661.

5 H. Nikmanesh, M. Moradi, G. H. Bordbar and R. S. Alam, *Ceram. Int.*, 2016, **42**, 14342–14349.

6 M. Pardavi-Horvath, *J. Magn. Magn. Mater.*, 2000, **215**, 171–183.

7 S. Azhagushanmugam, N. Suriyanarayanan and R. Jayaprakash, *Phys. Procedia*, 2013, **49**, 44–48.

8 K. K. Kefeni, T. A. Msagati and B. B. Mamba, *Mater. Sci. Eng., B*, 2017, **215**, 37–55.

9 C. Chinnasamy, A. Narayanasamy, N. Ponpandian, K. Chattopadhyay, K. Shinoda, B. Jeyadevan, K. Tohji, K. Nakatsuka, T. Furubayashi and I. Nakatani, *Phys. Rev. B: Condens. Matter Mater. Phys.*, 2001, **63**, 184108.

10 Z. Kargar, S. Asgarian and M. Mozaffari, *Nucl. Instrum. Methods Phys. Res., Sect. B*, 2016, **375**, 71–78.

11 S. Ghosh, P. Nambissan and R. Bhattacharya, *Phys. Lett. A*, 2004, **325**, 301–308.

12 A. Mukherjee, M. Banerjee, S. Basu, P. Nambissan and M. Pal, *J. Phys. D: Appl. Phys.*, 2013, **46**, 495309.

13 T. Prabhakaran and J. Hemalatha, *Ceram. Int.*, 2016, **40**, 3315–3324.

14 M. Rahimi, P. Kameli, M. Ranjbar, H. Hajihashemi and H. Salamati, *J. Mater. Sci.*, 2013, **48**, 2969–2976.

15 F. Saffari, P. Kameli, M. Rahimi, H. Ahmadvand and H. Salamati, *Ceram. Int.*, 2015, **41**, 7352–7358.

16 J. S. Ghodakea, R. C. Kambale, T. J. Shinde, P. K. Maskar and S. S. Suryavanshi, *J. Magn. Magn. Mater.*, 2016, **401**, 938–942.

17 M. N. Akhtar, M. A. Khan, M. Ahmad, M. S. Nazir, M. Imran, A. Ali, A. Sattar and G. Murtaz, *J. Magn. Magn. Mater.*, 2017, **421**, 260–268.

18 B. P. Rao and O. F. Caltun, *J. Optoelectron. Adv. Mater.*, 2006, **8**, 995.

19 C. Pascual-Izarra, A. W. Dong, S. J. Pas, A. J. Hill, B. J. Boyd and C. J. Drummond, *Nucl. Instrum. Methods Phys. Res., Sect. A*, 2009, **603**, 456–466.

20 B. H. Toby, *Powder Diffr.*, 2006, **21**, 67–70.

21 A. S. Group, *Database of Ionic Radii*, 1976, http://www.abulafia.mt.ic.ac.uk/shannon/ptable.php.

22 S. Karimi, P. Kameli, H. Ahmadvand and H. Salamati, *Ceram. Int.*, 2016, **42**, 16948–16955.

23 A. M. Wahba and M. B. Mohamed, *Ceram. Int.*, 2014, **40**, 6127–6135.

24 R. Valenzuela, *Magnetic ceramics*, Cambridge University Press, vol. 4, 2005.

25 R. Krause-Rehberg and H. S. Leipner, *Positron annihilation in semiconductors: defect studies*, Springer Science & Business Media, vol. 127, 1999.

26 F. A. Selim, M. H. Weber, D. Solodovnikov and K. G. Lynn, *Phys. Rev. Lett.*, 2007, **99**, 085502.

27 F. A. Selim, D. Solodovnikov, M. H. Weber and K. G. Lynn, *Appl. Phys. Lett.*, 2007, **91**, 104105.

28 G. Yuan, C. Li, J. Yin, Z. Liu, D. Wu and A. Uedono, *J. Phys. D: Appl. Phys.*, 2012, **45**, 445305.

29 C. Hiibner, T. Staab and R. Krause-Rehberg, *Appl. Phys. A: Mater. Sci. Process.*, 1995, **61**, 203–206.

30 P. J. Schultz and K. G. Lynn, *Rev. Mod. Phys.*, 1988, **60**, 701.

31 P. Nambissan, C. Upadhyay and H. Verma, *J. Appl. Phys.*, 2003, **93**, 6320–6326.

32 S. Chakraverty, S. Mitra, K. Mandal, P. Nambissan and S. Chattopadhyay, *Phys. Rev. B: Condens. Matter Mater. Phys.*, 2005, **71**, 024115.

33 F. Tuomisto and I. Makkonen, *Rev. Mod. Phys.*, 2013, **85**, 1583.

34 Y. Mohammadifar, H. Shokrollahi, Z. Karimi and L. Karimi, *J. Magn. Magn. Mater.*, 2014, **366**, 44–49.

35 A. Pradeep, P. Priyadharsini and G. Chandrasekaran, *J. Magn. Magn. Mater.*, 2008, **320**, 2774–2779.

36 B. Evans and S. Hafner, *J. Phys. Chem. Solids*, 1968, **29**, 1573–1588.

37 D. Neupane Dipesh, L. Wang, H. Adhikari, J. Alam and S. R. Mishra, *J. Alloys Compd.*, 2016, **688**, 413–421.

38 G. Tang, D. Ji, Y. Yao, S. Liu, Z. Li, W. Qi, Q. J. Han, X. Hou and D. L. Houless, *Appl. Phys. Lett.*, 2011, **98**, 072511.

39 D. Mane, U. Devatwal and K. Jadhav, *Mater. Lett.*, 2000, **44**, 91–95.

40 M. Gabal, S. Kosa and T. Almutairi, *J. Magn. Magn. Mater.*, 2014, **356**, 37–41.